Published in final edited form as:
IEEE Trans Robot. 2013 June 25; 29(5): 1139–1151. doi:10.1109/TRO.2013.2266754.

3-D Localization Method for a Magnetically Actuated Soft Capsule Endoscope and Its Applications

Sehyuk Yim [Student Member, IEEE] and
Department of Mechanical Engineering, Carnegie Mellon University, Pittsburgh, PA 15213 USA (samy@cmu.edu)

Metin Sitti [Senior Member, IEEE]
Department of Mechanical Engineering, Carnegie Mellon University, Pittsburgh, PA 15213 USA (sitti@cmu.edu)

Abstract

In this paper, we present a 3-D localization method for a magnetically actuated soft capsule endoscope (MASCE). The proposed localization scheme consists of three steps. First, MASCE is oriented to be coaxially aligned with an external permanent magnet (EPM). Second, MASCE is axially contracted by the enhanced magnetic attraction of the approaching EPM. Third, MASCE recovers its initial shape by the retracting EPM as the magnetic attraction weakens. The combination of the estimated direction in the coaxial alignment step and the estimated distance in the shape deformation (recovery) step provides the position of MASCE in 3-D. It is experimentally shown that the proposed localization method could provide 2.0–3.7 mm of distance error in 3-D. This study also introduces two new applications of the proposed localization method. First, based on the trace of contact points between the MASCE and the surface of the stomach, the 3-D geometrical model of a synthetic stomach was reconstructed. Next, the relative tissue compliance at each local contact point in the stomach was characterized by measuring the local tissue deformation at each point due to the preloading force. Finally, the characterized relative tissue compliance parameter was mapped onto the geometrical model of the stomach toward future use in disease diagnosis.

Keywords

Capsule endoscopy; localization; magnetic microrobot; soft robotics

I. Introduction

Currently, magnetic capsule endoscopy is one of the most promising medical technologies for noninvasive diagnosis on the upper gastrointestinal (GI) tract [1]–[3]. Many groups have demonstrated magnetic maneuvering of such magnetic capsules [4]–[6]. Hong *et al.* showed the feasibility of a magnetically actuated capsule in a pig's esophagus, stomach, and large intestine using a multi-degree-of-freedom robotic manipulator [7], [8]. Recently, Carpi and Pappone conducted an animal experiment of a magnetic capsule endoscope using a commercial permanent magnet-based actuation system (Niobe, Stereotaxis, Inc., St. Louis, MO, USA), which is mainly used for magnetic navigation of cardiovascular active catheters

[9]. Although the performance of this capsule's translational movement was limited due to uncontrollable field gradients, it could be resolved in the near future by using an electromagnetic actuation system or changing capsule locomotion dynamics [10]–[13].

As an alternative to existing rigid magnetic capsule endoscopes with only basic locomotion demonstrations, in our previous study, we proposed a magnetically actuated soft capsule endoscope (MASCE), which moves on the bottom surface of stomach using rolling locomotion [14], [22]. MASCE has two major characteristics. Next, MASCE's axial contraction can be used for an extra degree-of-freedom actuation and also for advanced therapeutic functions such as targeted or semi-implantable drug release [15]. However, such soft capsule's 3-D localization was a significantly challenging task. Even though various localization methods have been proposed for magnetic capsule endoscopes [16]–[19], they cannot be applied to MASCE and its platform for two reasons. First, external (off-board) Hall effect sensor arrays [16] are not compatible with the MASCE system where an external magnet is used for actuation. Next, using on-board Hall effect sensors is very challenging to measure the external magnetic field accurately because the internal magnetic field, which changes continuously during axial shape deformation of MASCE, infringes significantly with the external magnetic fields. Therefore, we introduce a new 3-D localization method for MASCE. The key concept is to use the magnetically actuated shape deformation and recovery to localize MASCE between each rolling locomotion cycles. Fig. 1 presents three main contents of this paper: 3-D localization method, 3-D mapping of the stomach, and characterization of the local, relative tissue compliance. They are connected to each other as shown in Fig. 2.

As the outline of this paper, Section II gives an overview of MASCE and the magnetic actuation platform. Section III presents the 3-D localization method and analysis using shape deformation and recovery. Section IV shows experiments to validate the performance of the proposed localization method. Additionally, this paper proposes two applications of 3-D localization of MASCE in Section V: tissue compliance estimation and reconstruction of 3-D map of the stomach. Experimental results of such potential applications and their possible clinical applications are discussed in Sections V and VI, respectively.

II. System Overview

The proposed magnetic endoscopy system consists of MASCE and an external magnetic actuation system. The detailed mechanical configuration of MASCE was given in [14]. Fig. 3 shows a CAD model of MASCE, which is modified to implement the proposed 3-D localization method. Two internal magnets are embedded at both ends of MASCE, and they are connected by four side linkages with three flexure hinges. MASCE has one monoaxial Hall effect sensor (A1302, Allegro, sensitivity = 1.3 mV/G) between two internal magnets. The embedded Hall effect sensor measures the magnetic field ($B_{ext} + B_{int}$) in the length direction of MASCE. A small secondary magnet (diameter: 3.2 mm and thickness: 0.8 mm) is located right under the Hall effect sensor. The magnetization direction of the secondary magnet is opposite to that of large internal magnets. Due to the superposition effect of magnetic fields [25], the maximum measurable magnetic field is extended up to 0.23 T.

The external magnetic actuation platform includes an external permanent magnet (EPM), which is moved by a motorized 5-degree-of-freedom stage (*XYZ*-$\theta\Phi$) under the patient's bed. This configuration separates the patient from the workspace of the EPM robotic manipulator; therefore, the unpredicted conflict between the patient and the EPM robotic manipulator can be avoided. MASCE moves on the bottom of the stomach surface using rolling motion. On such a slippery stomach surface, its workspace could be limited within a gentle slope (±25°) area [14]. Therefore, the assistive motion of the patient's bed is required to expand the limited workspace to the entire surface of the stomach.

III. Three-Dimensional Localization Method

Fig. 3 shows the three-step procedure to localize MASCE in 3-D during its rolling locomotion. The first step is the coaxial alignment stage (b). In this step, the magnetization direction of the internal magnets inside MASCE, the magnetization direction of EPM, and the center-to-center line between MASCE and EPM are aligned in one line. The second step is MASCE's shape deformation stage (c). As EPM approaches MASCE along the EPM's axial direction, MASCE is axially contracted because the magnetic attraction between EPM and the (upper) internal magnet of MASCE becomes strengthened. The last step is MASCE's shape recovery stage (d). In this step, as EPM becomes further from MASCE, MASCE recovers its initial shape. All these stages are detected by the output of the embedded Hall effect sensor of MASCE shown in Fig. 3. In this section, the principle and the role of each step for 3-D localization are introduced using experiments and simulations.

MASCE is localized twice via an EPM between each rolling locomotion cycles. Because the EPM's position and orientation are known, if the relative position of MASCE from EPM is estimated, MASCE's position in the absolute coordinate is calculated. Assuming that the relative coordinate is the spherical coordinate as in Fig. 3(a), direction of MASCE and the distance between MASCE and EPM are required to localize MASCE. The key equation for 3-D localization of MASCE is

$$C = P_0 + (D+L)\,\vec{a} \quad (1)$$

where C is the 3-D positions of MASCE, P_0 is the initial 3-D position of EPM at the coaxial alignment stage, $\vec{a}$ is the unit vector in the magnetization direction of EPM after the coaxial alignment stage as shown in Fig. 3(b), D is the critical distance between EPM and MASCE for shape deformation or recovery, and L is the displacement of EPM along the coaxial direction as shown in Fig. 3(c) and (d).

Differing from other approaches [16]–[19], the proposed localization method is based on the state of MASCE. This is a critical feature. The states of MASCE are divided into four as in Fig. 3 by the changing trend of the Hall effect sensor output. Because the shape deformation and the recovery of MASCE are activated when the pure external magnetic field becomes certain values, we do not need to calculate it in a complicated method. We can know the position of MASCE only at the two moments, but the effect of EPM on the embedded Hall effect sensor is not an issue any more. In the following sections, the direction estimation and the distance estimation methods are introduced.

A. Coaxial Alignment

In the coaxial alignment stage, the direction of MASCE from EPM in the spherical coordinate is estimated by orienting EPM in the θ- and Φ-directions. When MASCE becomes aligned with EPM in one axis as in Fig. 3(b), the output of the embedded Hall effect sensor is maximized. This stage gives information about $\vec{a}$, which is defined by

$$\vec{a}=(sin\ \phi_{cx}\ cos\ \theta_{cx},\ sin\ \phi_{cx}\ sin\ \theta_{cx},\ cos\ \phi_{cx}) \quad (2)$$

where Φ_{cx} and θ_{cx} are the converged angles of EPM during the coaxial alignment stage. In this section, the working principle, the implementation method, and the preliminary experimental results are introduced in detail.

1) Magnetic Field Analysis—Fig. 4(a) shows the coordinate to analyze the magnetic field of MASCE in the coaxial alignment stage. Assuming that the position of MASCE is (x_c, y_c, z_c) in Cartesian coordinates, it can be transformed to (r_c, Φ_c, θ_c) into spherical coordinates. If the distance (r_c) is assumed constant, the direction of MASCE is presented as (Φ_c, θ_c). Assuming that the EPM's magnetization direction is (Φ, θ), the misalignment angle (α) is calculated by (3) using the second law of cosine:

$$\alpha=arccos\left(1-\frac{1}{2}\left[(sin\ \phi_c\ cos\ \theta_c-sin\ \phi\ cos\ \theta)^2+(sin\ \phi_c\ sin\ \theta_c-sin\ \phi\ sin\ \theta)^2+(cos\ \phi_c-cos\ \phi)^2\right)\right). \quad (3)$$

The geometrical meaning of α is the geodesic angle between $\vec{a}$ and $\vec{c}$.

If the EPM is simplified to a single magnetic dipole, the maximum magnetic field of MASCE is presented as

$$max\,(B\,(\alpha))=\frac{\mu_0}{4\pi r_c^3}V_{epm}M_{epm}\left(1+3\ cos^2\ \alpha\right) \quad (4)$$

where M_{epm} is the EPM magnetization, V_{epm} is the EPM volume, r_c is the distance between EPM and MASCE, and μ_0 is the permeability of the air. As MASCE is automatically aligned with the maximum external magnetic field direction, the external magnetic field in the MASCE's magnetization direction is expressed as (5), which shows that the magnetic field is maximized to have the misalignment angle 0 such that

$$B_c\,(\alpha)=max\,(B\,(\alpha))=\frac{\mu_0}{4\pi r_c^3}V_{epm}M_{epm}\left(1+3\ cos^2\ \alpha\right). \quad (5)$$

At the global maximum of $B_c(\Phi, \theta)$, two partial derivatives satisfy

$$\frac{\partial B_c}{\partial\theta}=0,\quad \frac{\partial B_c}{\partial\phi}=0 \quad (6)$$

which result in two analytical solutions. The first one is that Φ is 0. If EPM is in the vertical direction, the rotation in the θ-direction is meaningless because EPM is axis-symmetric. However, the first solution is not the desired one because the magnetic field is not actually

maximized at this position. The second solution is that Φ and θ are Φ_c and θ_c, respectively, which means the EPM's final directions are same as the MASCE's directions.

Fig. 4(b) shows numerical simulations about the coaxial alignment. Assuming that (Φ_c, θ_c) is (30°, 60°), B_c was calculated as a function of (Φ, θ) using (3) and (5). The three routes of Fig. 4(b) show that, although their initial points (or the routes) were differently set, they finally converged to the same point (Φ_c, θ_c) through the coaxial alignment (compare routes 1, 2, and 3). Especially, the convergence following route 1 shows that EPM was orientated in the θ-direction and then in the Φ-direction. In such sequential orientation, the convergences in the θ-direction and in the Φ-direction are decoupled. This is analytically proved by (6). The partial derivatives of B_c about θ become zero only if θ is θ_c. If θ is fixed at θ_c, the partial derivative of B_c about Φ also becomes 0 only where Φ is Φ_c.

2) Modeling and Analysis—MASCE experiences the external magnetic torque and attraction, and the gravitational torque. Fig. 5 shows a free-body diagram of MASCE during the coaxial alignment stage. Assuming that MASCE is fixed at the same position and only tilted by magnetic interactions and the gravitational torque [14], the governing equation is expressed as

$$T_{\text{net}} = \left(\overrightarrow{F}_m \times 0.5L\,\overrightarrow{l}_{msc}\right) + \left(m_{msc}\overrightarrow{g} \times 0.5L\,\overrightarrow{l}_{msc}\right) + \left(V_{msc}\overrightarrow{M}_{msc} \times \overrightarrow{B}_{epm}\right) \quad (7)$$

where m_{msc} and V_{msc} are the mass and the volume of the internal magnet, respectively, $\boldsymbol{l}_{\text{msc}}$ is the unit vector in the MASCE's length (L) direction, $\boldsymbol{M}_{\text{msc}}$ is the magnetization of the internal magnet, $\boldsymbol{F}_m$ is the magnetic attraction, and $\boldsymbol{B}_{\text{epm}}$ is the external magnetic field. The MASCE's orientation is fixed if the net torque is 0. The analytical solution of (7) is given as

$$\begin{aligned} sin \quad \phi_{\text{error}} &= \frac{0.5 m_{msc} g L \quad sin \quad \phi_{tilt}}{|B_{epm} V_{msc} M_{msc}| + 0.5 F_m L} \\ &\cong \frac{m_{msc} g L \quad sin \quad \phi_{tilt}}{|2 B_{epm} V_{msc} M_{msc}|} \end{aligned} \quad (8)$$

where Φ_{tilt} and Φ_{error} are the tilt angle and the misalignment angle of MASCE, respectively. The first term of (7) is negligible because the magnetic attraction between EPM and MASCE is in the length direction. Equation (8) presents that the effect of gravitational torque in the coaxial alignment stage is limited. For example, if Φ_{tilt} is 30° and the external magnetic field is 0.05 T, the misalignment angle due to the gravitational torque is only about 1°.

3) Experiments—The accuracy of direction estimation in the coaxial alignment step was evaluated in preliminary experiments. First, MASCE was mounted on a rubber-coated substrate. Its position (x_c, y_c, z_c) was measured in Cartesian coordinates and transformed to (r, Φ_c, θ_c) in spherical coordinates. The cylindrical EPM was fixed at the origin and rotated in the Φ- and θ-directions. When the output of Hall effect sensor inside MASCE reached the maximum, the EPM's direction angles (Φ_{cx} and θ_{cx}) were measured. The final orientation of EPM was compared with (Φ_c, θ_c) in Table I. The misalignment error, which was calculated using (3), was about 5°. The experiments were repeated three times at the same setting to investigate the consistency of the results. The standard deviation of α was ± 1.2°.

The coaxial alignment should be precise because a small direction error could induce a large localization error as the distance from EPM to MASCE increases. Through experiments, we observed that the geometry of EPM plays an important role to minimize the error. As a cylindrical (or rectangular) magnet has a flat surface on its top, the sensitivity significantly decreases as the EPM becomes more aligned with MASCE. The most preferable geometry of EPM is a spherical magnet. Such shape would have a strong magnetic field in its axial direction. Therefore, in 3-D localization experiments of Section IV, a *spherical* magnet was used.

B. Shape Deformation and Recovery

While coaxial alignment is the process to estimate the direction of MASCE from EPM in spherical coordinates, the shape deformation and recovery of MASCE is the process to estimate the coaxial distance from EPM to MASCE. Due to the internal magnetic attraction, MASCE experiences shape deformation and recovery cycle with hysteresis as in Fig. 6(a). If the magnetic attraction between the upper internal magnet of MASCE and EPM exceeds the critical force of shape deformation (F_{dfm}), MASCE is abruptly compressed. In addition, if the magnetic attraction falls below the critical force (F_{rcv}) of shape recovery, MASCE recovers its initial shape abruptly. Shape deformation or recovery of MASCE is detected by the on-board Hall effect sensor because the internal magnetic field dramatically increases (or decreases) during such deformation (or recovery).

The critical distances for shape deformation and recovery (D_{dfm} and D_{rcv}) can be expressed as

$$\frac{F_{dfm}}{M_i V_i} = \frac{dB_{epm}}{dr}\Big|^{r=D_{dfm}}, \quad \frac{F_{rcv}}{M_i V_i} = \frac{dB_{epm}}{dr}\Big|^{r=D_{rcv}} \tag{9}$$

where $\boldsymbol{M}_i$ and V_i are the magnetization and the volume of the upper internal magnet, respectively, and r is the coaxial direction vector. D_{dfm} and D_{rcv} are governed by the EPM's size and magnetization, and the design (compliance) of MASCE, and plugged into D of (1) to localize MASCE.

1) Modeling and Analysis—MASCE on a tissue surface can be modeled as a serially connected mass–spring system, as shown in Fig. 6(c). Such a system's governing equation is expressed as

$$\begin{bmatrix} F_{mag}^{up} \\ F_{mag}^{low} \end{bmatrix} = \begin{bmatrix} m_{up} & 0 \\ 0 & m_{low} \end{bmatrix} \begin{bmatrix} \ddot{x}_{up} \\ \ddot{x}_{low} \end{bmatrix} + \begin{bmatrix} k_{msc}(x) & -k_{msc}(x) \\ -k_{msc}(x) & k_{msc}(x) + k_{tss} \end{bmatrix} \begin{bmatrix} x_{up} \\ x_{low} \end{bmatrix} \tag{10}$$

where F_{mag}^{up} (F_{mag}^{low}) is the external magnetic attraction between EPM and the upper (lower) internal magnet, k_{msc} is the stiffness of MASCE, and k_{tss} is the tissue stiffness.

Fig. 6(a) and (10) explain all the MASCE's behavior at the shape deformation and recovery moments theoretically. First, during O-P_a-P_b, P_c-P_d, and P_a-O of Fig. 6(a), the mass–acceleration term is negligible because the two masses move slowly. The upper row term of

(10) shows that the compression of MASCE ($x_{up} - x_{low}$) is governed by F_{mag}^{up}. The lower row term presents that the tissue is deformed by the sum of F_{mag}^{up} and F_{mag}^{low}.

Next, during P_b-P_c and P_d-P_a, k_{msc} becomes 0; in Fig. 6, the gradient at each position presents the compliance (k^{-1}) of MASCE. If F_{mag}^{up} becomes F_{dfm}, F_{dfm} is totally transferred to the mass–acceleration term of (10). The dominant acceleration term means the upper head of MASCE is abruptly compressed. In addition, because x_{low} moves slowly (i.e., slow deformation of the tissue), only F_{mag}^{low} governs the deformation of the tissue. Defining F_{mag}^{low} at the shape deformation moment as F_{dfm}^{P}, F_{dfm}^{P} and the recovery force of tissue ($k_{tss}\, x_{low}$) are in equilibrium. If the tissue is compliant (low k_{tss}), the deformation of the tissue is large. At a stiff tissue (high k_{tss}), the displacement of the lower head (x_{low}) is small. The above interpretation is also valid for F_{rcv} and F_{rcv}^{P} in the shape recovery stage.

The stiffness of MASCE becomes 0 when the increasing (or decreasing) inner magnetic attraction and the recovery force of the deforming side linkages are in equilibrium in the shape deformation (or recovery) stage. Therefore, the tissue stiffness does not affect F_{dfm} and F_{rcv}. D_{dfm} and D_{rcv} are also invariant in the same design and the same magnetic specifications of MASCE and EPM. As a result, F_{dfm}^{P} and F_{rcv}^{P} are also consistent as F_{dfm} and F_{rcv}, respectively.

2) Robustness Analysis—MASCE is magnetically actuated on the bottom surface of stomach and localized via EPM between each rolling locomotion steps. However, the entire stomach can be periodically disturbed by patient's breathing (15–20 breaths/min) and the force disturbance could affect the characteristic shape deformation and recovery behavior. In order to reflect this environmental factor, the robustness of D_{dfm} and D_{rcv} should be investigated. First, the magnetic field of EPM in its magnetization direction is expressed as

$$B_e(r) = \frac{\mu_0 M_{epm} V_{epm}}{\pi r^3} \quad (11)$$

where r is the distance from EPM and MASCE. The combination of (9) and (11) gives

$$\frac{F_{dfm} + F_d}{F_{dfm}} = \frac{(D_{dfm})^4}{(D_{dfm} + \Delta D_{dfm})^4} \quad (12)$$

where F_d is the force disturbance, and ΔD_{dfm} is the change of D_{dfm}. If (12) is normalized, the relation between the disturbance and the change of the shape deformation distance can be given as

$$\left(1 + \frac{\Delta D_{dfm}}{D_{dfm}}\right)^{-1} = \sqrt[4]{1 + \frac{F_d}{F_{dfm}}}. \quad (13)$$

Equation (13) is plotted in Fig. 7. By 10% of the force disturbance, the shape deformation (recovery) distance decreases 2.5%. If D_{dfm} is 300 mm and the force disturbance is 10% of F_{dfm}, MASCE is axially contracted when the distance is 292.5 mm.

3) Experiments—Consistency of D_{dfm} and D_{rcv} was experimentally evaluated. Experimental setup is shown in Fig. 10 and described in detail in Section IV. Without touching MASCE, it was aligned with EPM in the coaxial alignment step, and then, EPM was vertically moved using the linear actuator. The distance from the center of EPM to the bottom of MASCE was measured when MASCE was abruptly compressed and recovered.

Table II shows the summarized specifications of the internal magnets of MASCE, EPM, and the experimental critical distances. The important feature of this measurement is consistency of D_{dfm} and D_{rcv}. The standard deviations of D_{dfm} and D_{rcv} during ten times of measurements were only 0.15 and 0.24 mm, respectively. This consistency shows that the distance estimation using the empirical shape deformation (recovery) distance is reliable. We also measured D_{dfm} and D_{rcv} of a MASCE on a compliant substrate (e.g., silicone rubber or polyurethane) or changed the approaching speed of EPM to observe the effect of substrate compliance or the dynamic condition, respectively. However, the results were the same as the results on a rigid substrate, which are consistent with the expectations in modeling.

As shown in Table II, D_{dfm} and D_{rcv} are relatively short, 44.2 and 57.2 mm, respectively. In clinical applications, these distances should be longer than 300 mm for capsule endoscopy of obese patients. One way to increase D_{dfm} and D_{rcv} is making MASCE more compliant so that it can experience the shape deformation and recovery at lower external magnetic field gradients. The second way is to use a larger EPM with a stronger magnetization. Analytical magnetic model shows that D_{dfm} and D_{rcv} can be extended to about 300 mm if the diameter of EPM ($M_{epm} = 1.1 \times 10^6$ A/m) is 300 mm and F_{dfm} decreases by 50%.

C. Compatibility With Rolling Locomotion

In general, the remote control of MASCE consists of three steps. First, it is localized using the proposed method. Next, considering its current and target positions, the path of EPM is planned. Finally, using translation and rotation of EPM, it is navigated to the desired position. In this section, rolling locomotion and 3-D localization are executed step-by-step in simulations. Fig. 8 shows the captured images of the simulations in sequence. The red dots (C) and the blue dots (G) on the top surface of the cube mean the localized position and the goal position of MASCE, respectively. The black lines show the position and the orientation of EPM. The line length (10 mm) means the diameter of the spherical magnet.

First, the initial position of MASCE is C_0 and EPM is operated under MASCE. Assuming that the goal position of MASCE is G_1, EPM translates toward G_1 while being rotated [see Fig. 8(a)]. As soon as EPM reaches G_1, the coaxial alignment process starts. EPM is rotated in the θ-direction first [see Fig. 8(b)] and then in the Φ-direction [see Fig. 8(c)]. After the coaxial alignment stage, EPM is moved along the coaxial direction and MASCE is localized using D_{dfm} and D_{rcv} [see Fig. 8(c)]. At this stage, the exact position of C_1 is calculated. The next step is divided into two. If MASCE tracks EPM very well, MASCE and EPM's *XY*

positions are aligned before the next rolling locomotion [see Fig. 8(d)]. After the *XY* alignment, EPM moves toward the next goal G_2 while being rotated, again [see Fig. 8(e)]. However, if the tracking error of MASCE is significant, it means that MASCE is actuated toward a slope. In this case, right after the coaxial alignment, EPM is moved backward to locate MASCE within the desired workspace again [see Fig. 8(f)].

Fig. 9(a) shows EPM's Φ and θ during rolling locomotion, 3-D localization, *XY* alignment, and steering. The detailed description of each stage is as follows.

1. *Rolling Locomotion:* θ is constant because it is to steer EPM in the *XY* plane. Only Φ changes for rolling motion [see EPM's behavior in Fig. 8(a)].
2. *Coaxial Alignment:* Basically, the coaxial alignment can start anytime except for $\Phi = 0$ during rolling motion. This is because, when Φ is 0, the gradients about Φ and θ become 0 (see Section III-A for detailed information). Normally, the coaxial alignment starts when EPM is tilted 20–30° about the horizontal surface. EPM is aligned with MASCE by rotation in the θ-direction first and then in the Φ-direction.
3. Shape Deformation and Recovery of Magnetically Actuated Soft Capsule Endoscope: After coaxial alignment, EPM is moved along the coaxial direction and MASCE is deformed and recovered. Both Φ and θ do not change during this stage. Only EPM moves back and forth in its magnetization direction.
4. *XY Alignment:* After 3-D localization of MASCE, EPM's position is aligned with MASCE's center in the *XY* plane. Φ slightly changes during this alignment.
5. *Steering:* Only EPM's θ changes toward the next goal (G_2) of MASCE. While EPM is rotated in the θ-direction, Φ is 0. After steering, the second rolling locomotion starts.
6. *Backward Rolling Locomotion:* Fig. 9(b) shows that (after the 3-D localization) EPM moves backward in order to locate MASCE in the workspace. θ is constant, and only Φ changes for the rolling motion of EPM.

IV. Experiments

A. Experimental Setup and Procedure

In this section, experimental results are introduced to evaluate the accuracy of the proposed 3-D localization method. Fig. 10 shows the experimental setup, which consists of two parts. First, the lower part is for manipulation of EPM. The spherical EPM is rotated about two axes (θ and Φ) for the coaxial alignment. Two protractors with a resolution of 1° are used to measure θ and Φ. The spherical magnet is moved in the coaxial direction ($\vec{a}$) by a motorized linear actuator (MFA-CC, Newport, RI, USA) in shape deformation and recovery steps [see the movement of EPM in Fig. 8(b) and (c)]. The displacement (resolution: 1 μm) of EPM moved by the linear actuator is connected as input in a data acquisition board (National Instruments, PCIe-6321).

Next, the upper part consists of a substrate with a silicone rubber stomach model, a substrate holder, and a webcam. The substrate can be moved in three directions (X_{rel}, Y_{rel}, Z_{rel}) and

rotated about two axes (Φ_s, θ_s). Because the substrate's position and orientation are differently set by changing five variables (x_{off} , y_{off} , z_{off}, Φ_{off}, θ_{off}), even though EPM is fixed at the origin (P_0) during the coaxial alignment step, the relative position of MASCE on the substrate can be differently set. Thus, (1) is modified to

$$C^{rel}=T_{abs}^{rel}\cdot(D+L)\,\overrightarrow{a} \quad (14)$$

where T_{abs}^{rel} is the coordinate transformation matrix (4 × 4) between absolute coordinates and relative coordinates, D is D_{dfm} or D_{rcv} (see Table II), and L is the approaching (or retracting) distance of EPM in the coaxial direction during shape deformation and recovery stages, which is given by the linear actuator. Equation (14) shows that the absolute position of MASCE is transformed to the relative position on the substrate (compare (X_{rel}, Y_{rel}, Z_{rel}) and (X_{abs}, Y_{abs}, Z_{abs}) in Fig. 10).

The prototype and the CAD model of MASCE are shown in Figs. 1(a) and 3, respectively. The output of the Hall effect sensor is connected as input in the same data acquisition board, which is used to measure the displacement of the linear actuator. By measuring the magnetic field and the displacement of EPM simultaneously, accurate L_{dfm} and L_{rcv} values are measured during shape deformation and recovery steps, respectively. Nickel–chrome wires with a diameter of 70 μm were used to provide power to the Hall effect sensor and to measure the output. Because it is flexible and tough, the error due to the wire tension was negligible during the experiments.

B. Flat Substrate Experiments

First, the proposed 3-D localization method was evaluated on a flat, smooth, and rigid acrylic substrate. Instead of the rubber-made stomach model, a substrate with nine markers was mounted on the setup. MASCE prototype was located at nine different positions on the substrate. The coaxial alignment step was executed manually looking at the sensor output, which was displayed in a monitor because Φ and θ should be adjusted accordingly. MASCE's shape deformation and recovery were executed using the linear actuator (speed = 0.5 mm/s). During the experiments, the Hall effect sensor's output and the displacement of EPM were measured using the same data acquisition board. After experiments, the displacement (L_{dfm} or L_{rcv}) of EPM was read in the measured data considering the sensor output. As described in Fig. 3(c) and (d), the Hall effect sensor output abruptly increases or decreases at the shape deformation and the recovery moments. The experiments were repeated multiple times at each position to evaluate the standard deviation of the error.

Fig. 11(a) and (b) shows the localized MASCE using D_{dfm} and D_{rcv}, respectively. The "X" marks and the "O" marks represent the real and estimated positions of MASCE, respectively. The diameter of the circles means the standard deviation of the position error at each position, which presents the consistency of the precision. The results are summarized in Table III. The average error range was 2.0–3.7 mm. Because the effective distance between MASCE and EPM during the experiments was 56.7–69.7 mm, the normalized ratio between the error and the distance was 2.9–5.5%.

In Table III and Fig. 11, the shape recovery-based measured positions present a smaller error than the shape deformation-based ones. Experimental observations explain this trend. First, MASCE is more precisely aligned with the external magnetic field after the axial contraction because the magnetic torque becomes stronger as MASCE is more compressed. Next, the acrylic substrate is slightly deflected by the preloading force. Because F_{dfm}^{P} and F_{rcv}^{P} are 1.57 and 0.64 N, respectively, the substrate is more deflected in the shape deformation stage than in the shape recovery stage.

The time duration used for MASCE's coaxial alignment, shape deformation, and recovery in each experiment was about 1 min. The coaxial alignment was manually performed and EPM was slowly (1 mm/s) moved along the coaxis. If the coaxial alignment is automatically executed by a motorized setup and EPM is operated fast in the future, the time duration for executing 3-D localization would be reduced significantly.

C. Stomach Model Experiments

The second set of experiments was conducted using a synthetic stomach model [14]. The synthetic stomach model is made of silicone rubber (Dow Corning, HS II); therefore, the bottom surface of the model is deformed by the external magnetic attraction. This is similar to the tissue deformation and the organ rearrangement in the human abdomen.

First, the 3-D geometry of the stomach model was measured. Using a probe and a substrate with (*XY*) grid-hole patterns (center-to-center distance: 10 mm), the depth (Z) of synthetic stomach model at each grid was manually scanned. Fig. 12 shows the stomach modeling from the 3-D scanned data. Next, MASCE was located at 16 different positions of the rubber-made stomach model and localized using the proposed method. As shown in Fig. 12, the estimated contact points are lower than the actual surface of the 3-D model. Due to the deformation of the rubber-made stomach model, the position difference between the 3-D scanned stomach model and the localized contact points is larger than the error of the flat substrate experiments. Fig. 12 also shows two datasets: the shape deformation-based localization and the shape recovery-based localization. Because F_{rcv} is smaller than F_{dfm}, the stomach model is less deformed by MASCE at the shape recovery moment.

V. Three-Dimensional Mapping and Tissue Compliance Characterization

A. Tissue Compliance Estimation

MASCE is shown to preload and deform the tissue surface during 3-D localization using the external magnetic attraction. As introduced in Section III-B, the compliance of the tissue would be measured using the displacement of the tissue due to MASCE's preloading force (F_{dfm}^{P} and F_{rcv}^{P}). Here, we propose a procedure to measure the relative tissue stiffness quantitatively towards a new clinically useful elastography technique to diagnose cancerous areas inside the GI tract [23].

We assumed that the tissue deformation (recovery) curve is approximated by a simple polynomial function. To decide the order of the polynomial function, we investigated the empirical relation between the indentation depth of a deformable membrane and the

preloading force of the spherical indenter. Three membrane samples made of silicone rubber (HS II, Dow Corning) were prepared and indented. Fig. 13(a) shows the experimental result of sample A. The curve is divided into three stages: 1) preloading stage, 2) transition stage, and 3) relaxation stage. In the preloading stage, the force (F) can be approximately expressed as a quadratic form of the indentation depth (s) as

$$F_1 = k^* s^2 \quad (15)$$

where k^* is the effective stiffness coefficient at the contact point, and s is the displacement of the tissue. In the transition stage, the membrane experiences a stress relaxation. Even though the indentation depth of the membrane does not change, the actual normal force decreases because the stress of membrane is slowly relaxed inside the membrane. This is a common feature of a viscoelastic material. The magnitude of the stress reduction (f_0) depends on the transition time. As the transition time becomes longer, f_0 becomes larger. In the relaxation stage, the force is expressed as a quadratic form of the indentation depth again, which is given by

$$F_3 = k^* s^2 - f_0. \quad (16)$$

Here, the translational displacement (f_0) between F_1 and F_3 is due to the stress relaxation in the transition stage.

If the tissue deformations are, respectively, s_{dfm} and s_{rcv} when MASCE is axially contracted and relaxed, s_{rcv} and k^* can be given by

$$s_{rcv} = \frac{\Delta s}{\sqrt{F_{dfm}^p / (F_{rcv}^p + f_0)} - 1} \quad (17)$$

$$k^* = \frac{F_{rcv} + f_0}{s_{rcv}^2} \quad (18)$$

where Δs is the difference between s_{dfm} and s_{rcv}. These equations show that, if F_{dfm}^{P}, F_{rcv}^{P}, and Δs are known, it is possible to estimate not only the deformation of the tissue at the two moments but also the effective stiffness coefficient.

We evaluated the accuracy of the proposed compliance estimation method in experiments. The prepared three membranes were characterized by the proposed method. Δs was estimated by localizing MASCE on the sample A. The stiffness coefficient was estimated using (17) and (18). Because f_0 is unknown, it was differently set between 0 and 0.2 N. Fig. 13(b) shows the reconstructed stiffness curve of the membrane sample A. The indentation result (the discrete plot with the + marks) is similar to the reconstructed curve (colored by gray). Especially, the precision is dramatically improved if f_0 (0.1 N) is close to the actual range of the stress relaxation (0.09–0.12 N). k^* (0.021 N/mm^2) is the same as k_{cf} which was curve-fitted in the indentation experimental results. In addition, their hysteresis areas almost overlap.

The experiments were repeated using samples B and C as well. Table IV shows the summarized experimental results. The results present two points. First, even though f_0 is assumed to be 0, the relative comparison of the sample membrane stiffness is possible (see the fifth column). If f_0 is close to the actual stress relaxation of the tissue, the result becomes more accurate (compare k^* in the last column with k_{cf} in the second column). The actual stress relaxation of each sample is presented in the third column of Table IV.

B. Three-Dimensional Mapping of Local Tissue Surface

In this section, the second new application, i.e., 3-D mapping of the local stomach surface, is introduced. MASCE employs rolling-based surface locomotion by the external magnetic field. Therefore, the localized 3-D contact points of MASCE indicate the tissue surface of the stomach. If a number of contact points are connected each other, the rough geometry of the stomach could be reconstructed. However, due to the preloading force when MASCE is localized, only deformed stomach geometry can be estimated. For example, Fig. 12 shows that the contact points would give the inaccurate surface geometry of the stomach.

The above issue can be solved by compensating the deformation of the tissue surface using the reconstructed tissue compliance curve. s_{rcv} presents the deformation of the tissue surface. The calculated s_{rcv} is added on the shape deformation distance of (12) as

$$D_{rcv,com}=D_{rcv}+s_{rcv}. \quad (19)$$

Fig. 14 shows the reconstructed 3-D map of the rubber stomach model, which was implemented by applying (19). The rest of the area of the stomach surface was reconstructed by applying the surface fitting toolbox of MATLAB to the contact points. Compared with Fig. 12(b), the deformation-compensated 3-D map is more similar to the original geometry of the stomach simulator. The compensated displacement of the stomach surface ranges from 3.3 to 5.8 mm.

Three-dimensional mapping of the local tissue surface could be used for path planning of MASCE. The block diagram of Fig. 2 shows that the 3-D map is updated after rolling locomotion and an operator drives EPM, considering the updated 3-D map. For example, if MASCE is driven toward a side-wall or a steep slope, the EPM's path at the next step could be assigned in the backward space to move MASCE within the desired workspace. While reconstructing the 3-D map of a stomach using planar images is computationally expensive due to feature detection or optimization, the proposed 3-D mapping method results from the localized MASCE directly. Even though the proposed method does not contain a computational process, it provides the rough geometry for path planning of MASCE and EPM. Integrating simultaneous localization and mapping methods in mobile robotics with MASCE and the proposed localization method is a promising future work for 3-D mapping of complex surfaces such as the stomach.

C. Compliance Imaging of the Local Tissue Surface

The final step is to combine the estimated stiffness coefficient (k^*) with the reconstructed 3-D map. The procedure to build the compliance map is as follows. First, a polynomial

function ($k^* = g(x, y)$) is obtained using a surface fitting function. The compliance of the rest area of the stomach model is then estimated using this polynomial function. Finally, the calculated compliance is overlapped with the reconstructed 3-D map. Fig. 15 shows the colored map of the tissue compliance. The estimated stiffness coefficient k^* can be used as a parameter to compare the compliance of the tissue. The side area of the simulator is more compliant than the flat area at the center because that area is thinner.

The combination of the estimated tissue compliance and the reconstructed 3-D map of the local tissue surface could be used as a new elastography technique. Elastography is a noninvasive diagnosis method to estimate relative stiffness or strain of soft tissues in order to detect or classify tumors [20], [21], [23]. A tumor or an abnormal cancerous growth is normally 5–28 times stiffer than the surrounding normal soft tissue. When a mechanical force or vibration is applied, the tumor deforms less than the surrounding tissue. Currently, elastography is implemented via MRI, X ray, or ultrasound images. However, none of these techniques can give optical camera images in addition to the relative compliance map, as in the case of MASCE, where visual images are the most common information for doctors to diagnose diseases inside the stomach. Moreover, MASCE-based elastography could be much less expensive than the MRI-based elastography, much less noisy than the ultrasonic imaging (ultrasound imaging technique has drawbacks like low signal-to-noise ratio and the presence of strong wave reflectors such as bones and air pockets [24]) based elastography, and much less invasive than X-ray-based elastography, which exposes the patient to X-rays.

D. Requirements and Limitations

There are three following requirements for the precise 3-D localization of MASCE, 3-D mapping of the local tissue surface, and tissue compliance estimation.

1. The position of stomach has to be stable in the abdomen. It was already verified that a stomach filled with water fixes its location in the abdomen, which can reduce the organ rearrangement issue during magnetic actuation [13]. In some extreme cases, MASCE could slide on a slippery tissue surface during the shape deformation stage if it is pulled by the magnetic attraction at a slope (the boundary of the possible workspace). MASCE's such undesired movement after the coaxial alignment stage could be detected using on-board camera images of the capsule using optical flow or other image processing techniques. In this case, the localization method should start over from the coaxial alignment stage.

2. A large number of data points are required to reconstruct the meaningful geometrical model of stomach. In the experiments of Fig. 14, 16 contact points were used. The way to improve the resolution of the 3-D map is to down-size MASCE and actuate it delicately to cover the whole bottom area.

3. In order to estimate more accurate effective stiffness co-efficient, the stress relaxation (f_0) during the transition stage needs to be investigated. Currently, the effective stiffness coefficient should be estimated assuming that f_0 is 0. However, as shown in Fig. 13 and Table IV, if f_0 is estimated well, the accuracy of the stiffness coefficient would be dramatically improved. A possible solution is to use

an analytical tissue model describing the relation between the transition time and the stress relaxation. This will be a future work.

Basically, both tissue compliance estimation and 3-D mapping of the local tissue surface are enabled by 3-D localization of MASCE. Therefore, it is important to minimize the localization error to improve the accuracy of the 3-D map and the compliance estimation. Fig. 11 shows that the proposed localization method has inherent errors, which range from 2.0 to 3.7 mm. The error is mainly due to the coaxial alignment error. If MASCE is distant from EPM in practice, the localization error could dramatically increase. For example, if the distance between EPM and MASCE becomes five times, the position error could increase to five times of the original one. For a more precise coaxial alignment, the embedded Hall effect sensor should have a higher sensitivity, and its measurable magnetic field needs to be very high. Furthermore, possible disturbances such as the tether should be removed.

E. Compatibility With Localized Drug Release Function

The strength of MASCE is that it can also perform localized drug release type of therapeutic functions by its axial deformation control remotely [22]. To be able to implement localized drug release independently from 3-D localization, the critical forces for shape deformation (F_{dfm}), shape recovery (F_{rcv}), and drug release (F_{drg}) should be very distinct as in Fig. 16. If the stiffness of the drug chamber is high, the axial contraction during 3-D localization should not induce the undesired drug release. In the region **A** of Fig. 16, MASCE moves on the bottom surface of the tissue using rolling motion, and its position is estimated using its shape deformation and recovery. Localized drug release is triggered by a strong external magnetic field in region **B**. If the magnetic attraction is stronger than F_{drg}, the drug chamber is abruptly compressed, and the polymeric gel is released to coat a gastric ulcer [22]. Region **C** is the force margin that prevents the undesired drug release during rolling locomotion.

VI. Conclusion and Future Work

This paper has introduced a 3-D localization method for MASCE. The proposed method is based on MASCE's unique compliance feature where its shape is abruptly deformed and recovered at a certain level of the external magnetic attraction. The critical force for the shape deformation (recovery) is determined by MASCE's axial compliance and the internal magnetic attraction. Therefore, MASCE has its own characteristic shape deformation (recovery) distance, which is used to estimate the distance from EPM to MASCE. In the proposed method, MASCE can be localized between the rolling locomotion steps without a computational process requiring three-axial magnetic fields data. Therefore, the errors due to the inaccurate magnetic modeling of EPM, sensor noise, and sensor misalignment are avoided. The error of the proposed algorithm ranges from 2 to 4 mm with the given experimental conditions. The developed 3-D localization method is not directly compatible with other capsule endoscopes. However, the main idea of using the state change of the capsule for localization could be implemented in other magnetic capsule robots as well [26].

Two new applications enabled by 3-D localization were also proposed. The first one is a 3-D geometrical modeling of the stomach surface. Such mapping can be a reference for path planning of MASCE and EPM. In addition, it can be a database for disease development

analysis. The second application is to characterize the relative tissue compliance in-situ using the tissue deformation difference due to the preloading force at the contact (tissue) point. The estimated effective tissue stiffness coefficient can be used to detect a cancerous region. Future work will focus on building prototypes, as in Fig. 16, to implement the developed magnetic localization method and localized drug release independently. In addition, validating and improving the accuracy of the proposed 3-D localization, mapping, and elastography methods in more realistic environments (e.g., in *ex vivo* porcine stomach) is a future work.

Acknowledgments

This work was supported by in part by the National Institute of Health under Grant R01-NR014083.

Biographies

Sehyuk Yim (S'09) received the B.Eng. degree in mechanical engineering, the B.Eng. degree in electronic engineering in 2007, and the M.S. degree in mechanical engineering in 2009, all from Sogang University, Seoul, Korea, and Ph.D. degree in mechanical engineering from Carnegie Mellon University, Pittsburgh, PA, USA, in December 2012.

He has been a Postdoctoral Research Fellow with the Department of Mechanical Engineering, Carnegie Mellon University, since 2013. His current research interests include the design, modeling, and control of bioinspired robots, soft robots for medical applications, modular robots, and programmable matter.

Metin Sitti (S'94–M'99–SM'08) received the B.Sc. and M.Sc. degrees in electrical and electronics engineering from Bogazici University, Istanbul, Turkey, in 1992 and 1994, respectively, and the Ph.D. degree in electrical engineering from the University of Tokyo, Tokyo, Japan, in 1999.

He was a Research Scientist with the University of California at Berkeley, Berkeley, CA, USA, during 1999–2002. He is currently a Professor with the Department of Mechanical

Engineering and the Robotics Institute, Carnegie Mellon University, Pittsburgh, PA, USA. He is also the Director of the NanoRobotics Lab and the Center for Bio-Robotics. His research interests include bioinspired and biohybrid miniature mobile robots, medical microrobots, bioinspired micro/nano structures, and micro/nanomanipulation.

Dr. Sitti received the SPIE Nanoengineering Pioneer Award in 2011, the National Science Foundation CAREER Award in 2005, and the IBM Smarter Planet Award in 2012. He received the Best Paper Award at the IEEE/RSJ International Conference on Intelligent Robots and Systems in 1998 and 2009, the first prize at the World RoboCup Nanogram Demonstration League in 2012 and 2013, the Best Biomimetics Paper Award at the IEEE Robotics and Biomimetics Conference in 2004, and the Best Video Award at the IEEE Robotics and Automation Conference in 2002. He was appointed the Adamson Career Faculty Fellow during 2007–2010. He was the Vice President for Technical Activities of the IEEE Nanotechnology Council during 2008–2010. He was elected as a Distinguished Lecturer of the IEEE Robotics and Automation Society for 2006–2008. He is the current active Editor-In-Chief of the *Journal of Micro-Bio Robotics*.

References

[1]. Fireman Z, Glukhovsky A, Scapa E. Future of capsule endoscopy. Gastrointestinal Endoscopy Clinic. Jan; 2004 14(1):219–227.

[2]. Moglia A, Menciassi A, Dario P, Cuschieri A. Capsule endoscopy: Progress update and challenges ahead. Nature Rev. Gastroenterology Hepatology. Jun.2009 6:353–361.

[3]. Toennies JL, Tortora G, Simi M, Valdastri P, Webster RJ III. Swallowable medical devices for diagnosis and surgery: The state of the art. J. Mechanical Eng. Sci. 2010; 224(7):1397–1414.

[4]. Rey JF, Ogata H, Hosoe N, Ohtsuka K, Ogata N, Ikeda K, Aihara H, Pangtay I, Hibi T, Kudo S, Tajiri H. Feasibility of stomach exploration with a guided capsule endoscope. Endoscopy. 2010; 42(7):541–545. [PubMed: 20593331]

[5]. Swain P, Toor A, Volke F, Keller J, Gerber J, Rabinovitz E, Rothstein R. Remote magnetic manipulation of a wireless capsule endoscope in the esophagus and stomach of humans. Gastrointest. Endos. Jun; 2010 71(7):1290–1293.

[6]. Volke F, Keller J, Schneider A, Gerber J, Reimann-Zawadzki M, Rabinovitz E, Mousse CA, Swain P. In-vivo remote manipulation of modified capsule endoscopes using an external magnetic field. Gastrointest. Endos. 2008; 67:121–122.

[7]. Hong Y, Kim J, Kwon Y, Song S. Preliminary study of a twistable thread module on a capsule endoscope in a spiral motion. Int. J. Precision Eng. Manuf. 2011; 12(3):461–468.

[8]. Lee J, Kim B, Hong Y. A flexible chain-based screw propeller for capsule endoscopes. Int. J. Precision Eng. Manuf. 2009; 10(4):27–34.

[9]. Carpi F, Pappone C. Magnetic maneuvering of endoscopic capsules by means of a robotic navigation system. IEEE Trans. Biomed. Eng. May; 2009 56(5):1482–1490. [PubMed: 19174328]

[10]. Carpi F, Kastelein N, Talcott M, Pappone C. Magnetically controllable gastrointestinal steering of video capsules. IEEE Trans. Biomed. Eng. Feb; 2011 58(2):231–234. [PubMed: 20952324]

[11]. Kummer MP, Abbott JJ, Kratochvil BE, Borer R, Sengul A, Nelson BJ. OctoMag: An electromagnetic system for 5-DOF wireless micromanipulation. IEEE Trans. Robot. Dec; 2010 26(6):1006–1017.

[12]. Pawashe C, Floyd S, Sitti M. Modeling and experimental characterization of an untethered magnetic micro-robot. Int. J. Robot. Res. 2009; 28(8):1077–1094.

[13]. Keller, H.; Juloski, A.; Kawano, H.; Bechtold, M.; Kimura, A.; Takizawa, H.; Kuth, R. Method for navigation and control of a magnetically guided capsule endoscope in the human stomach; Proc. IEEE RAS/EMBS Int. Conf. Biomed. Robot. Biomechatronics; Jun. 2012; p. 859-865.

[14]. Yim S, Sitti M. Design and rolling locomotion of a magnetically actuated soft capsule endoscope. IEEE Trans. Robot. Feb; 2012 28(1):183–194.

[15]. Yim S, Sitti M. Shape-programmable soft capsule robots for semi-implantable drug delivery. IEEE Trans. Robot. Oct; 2012 28(5):1198–1202.

[16]. Hu C, Li M, Song S, Yang W, Zhang R, Meng MQ-H. Cubic 3-axis magnetic sensor array for wirelessly tracking magnet position and orientation. IEEE Sensors J. May; 2010 10(5):903–913.

[17]. Salerno M, Ciuti G, Lucarini G, Rizzo R, Valdastri P, Menciassi A, Landi A, Dario P. A discrete-time localization method for capsule endoscopy based on on-board magnetic sensing. Meas. Sci. Technol. 2012; 23:015701.

[18]. Kim J, Kwon Y, Hong Y. Automated alignment of rotating magnetic field for inducing a continuous spiral motion on a capsule endoscope with a twistable thread mechanism. Int. J. Precision Eng. Manuf. 2012; 13(1):31–37.

[19]. Natali C, Beccani M, Valdastri P. Real-time pose detection for magnetic medical devices. IEEE Trans. Magn. to be published. DOI: 10.1109/TMAG.2013.2240899.

[20]. Kim K, Johnson LA, Jia C, Joyce JC, Higgins PDR, Rangwalla S, Rubin JM. Non-invasive ultrasound elasticity imaging (UEI) on Crohn's disease: Animal model. Ultrasound Med. Biol. 2008; 34(6):902–912. [PubMed: 18294759]

[21]. Rubin JM, Xie H, Kim K, Weitzel WF, Emelianov SY, Aglyamov SR, Wakefield TW, Urquhart AG, O'Donnell M. Sonographic elasticity imaging of acute and chronic deep venous thrombosis in humans. J. Ultrasound Med. 2006; 25(9):1179–1186. [PubMed: 16929019]

[22]. Yim S, Goyal K, Sitti M. Magnetically actuated soft capsule with multi-modal drug release function. IEEE/ASME Trans. Mechatronics. to be published. DOI: 10.1109/TMECH. 2012.2235077.

[23]. [Online]. Available at http://en.wikipedia.org/wiki/Elastography

[24]. Nelson B, Kaliakatsos I, Abbott J. Microrobots for minimally invasive medicine. Annu. Rev. Biomed. Eng. Aug.2010 12:55–85. [PubMed: 20415589]

[25]. Cheng, DK. Field and Wave Electromagnetics. 2nd ed.. Addison-Wesley; Reading, MA, USA: 1992.

[26]. Popek, KM.; Mahoney, AW.; Abbott, JJ. Localization method for a magnetic capsule endoscope propelled by a rotating magnetic dipole field; Proc. IEEE Int. Conf. Robot. Autom.; May 2013; p. 5328-5333.

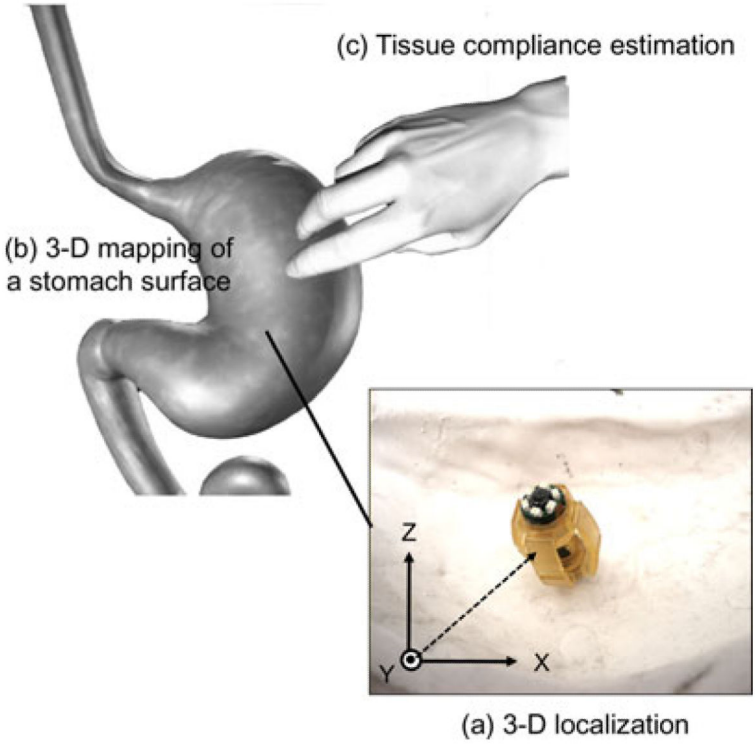

Fig. 1.

(a) Magnetically actuated soft capsule endoscope (MASCE) prototype, which is localized in 3-D by utilizing its shape deformation and recovery properties. Such a localization method enables (b) 3-D mapping of the stomach geometry and (c) local tissue compliance estimation (elastography) in addition to precise motion control of MASCE.

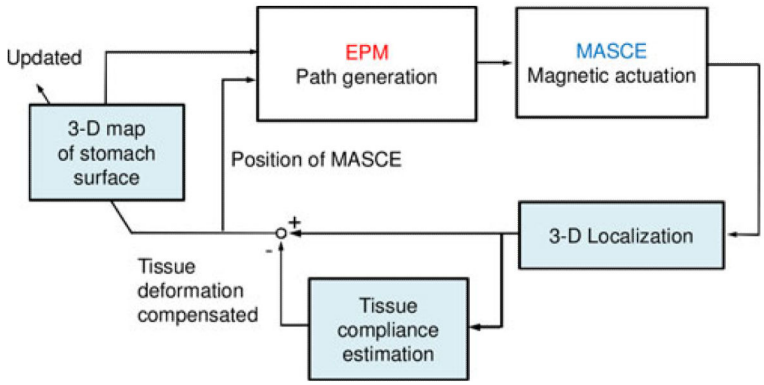

Fig. 2.

Block diagram for operation of MASCE while being moved, localized, and used for 3-D tissue compliance estimation and map generation; MASCE is actuated and rolled on the bottom surface of stomach by an EPM in 3-D [14] and localized using the proposed method in this study. Such 3-D localization information is used to measure the local stiffness of the stomach by measuring the tissue deformation. Compensating such tissue deformation, EPM's position is controlled, and a 3-D map of the stomach is created.

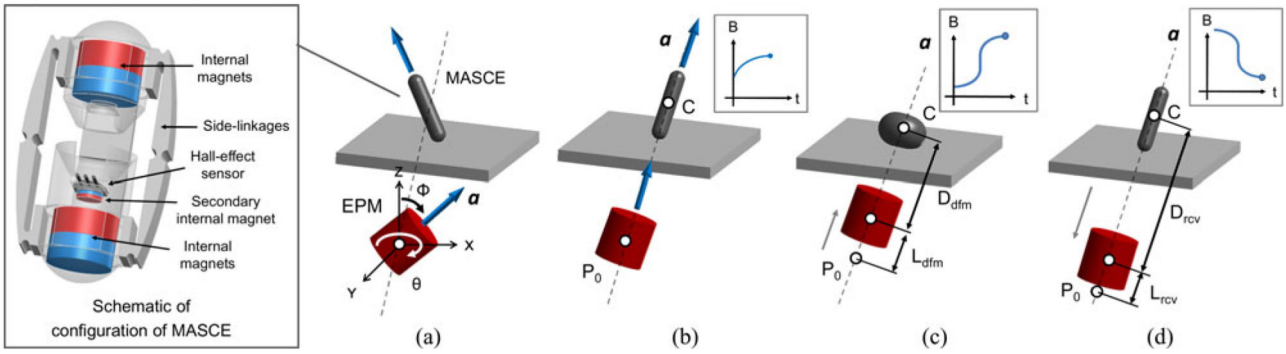

Fig. 3.

Schematic of component in MASCE and steps of 3-D localization estimation method. (a) Initial state of EPM and MASCE (gray arrow: magnetic field from the EPM; blue arrow: magnetization direction of magnets; gray dotted line: center-to-center line between EPM and MASCE). The orientation of EPM is given by its magnetization direction (***a***) and expressed by Φ and θ in the spherical coordinate. (b) Coaxial alignment stage where the output of the Hall effect sensor inside MASCE is maximized; the EPM's magnetization direction (***a***) becomes the coaxis of EPM and MASCE. P_0 is the initial 3-D position of EPM at the coaxial alignment stage. (c) Axial shape deformation and (d) shape recovery of MASCE by controlling the EPM's coaxial distance are used to measure the axial distance of MASCE from the EPM where the Hall effect sensor output (i.e., internal magnetic field) is suddenly increased or decreased due to the shape change. D_{dfm} and D_{rcv} are the critical distances inducing MASCE's shape deformation and recovery, respectively. L_{dfm} and L_{rcv} are the displacements of EPM in the coaxial direction until shape deformation and recovery occur, respectively.

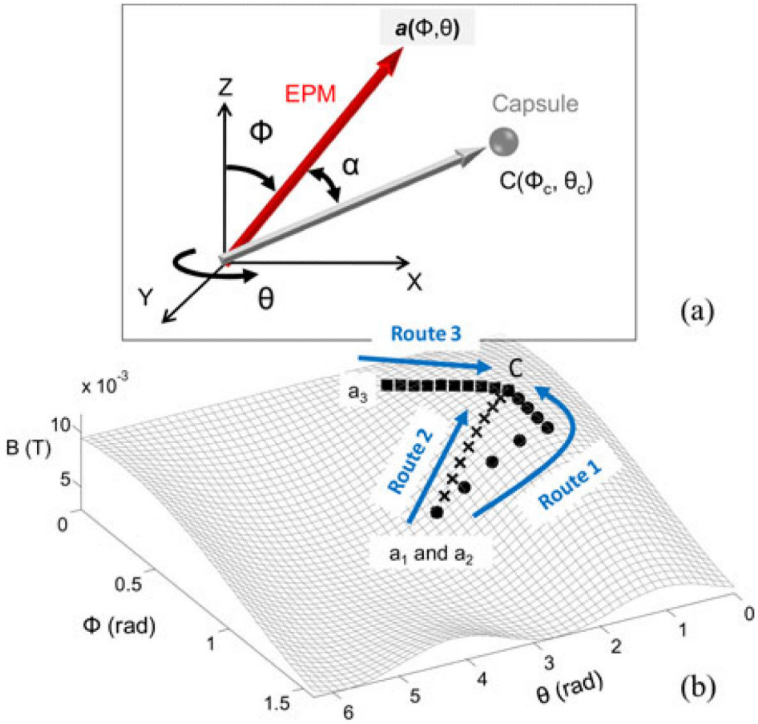

Fig. 4.

(a) Spherical coordinate to calculate the misalignment angle (α); a is the magnetization direction of EPM [its direction is expressed as (Φ, θ)]. C is the 3-D position of MASCE [its direction is expressed as (Φ_c, θ_c)]. (b) Simulations about the convergence of EPM starting from different initial directions (a_1 , a_2, and a_3) to C; a_1 and a_2: (45°, 155°); a_3: (10°, 120°); C: (30°, 60°). Three different convergence routes were assumed in simulations.

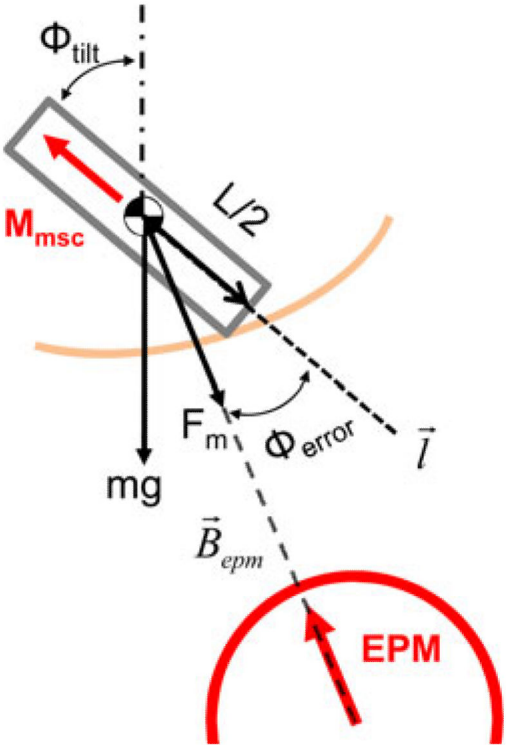

Fig. 5.
Free-body diagram of MASCE during coaxial alignment.

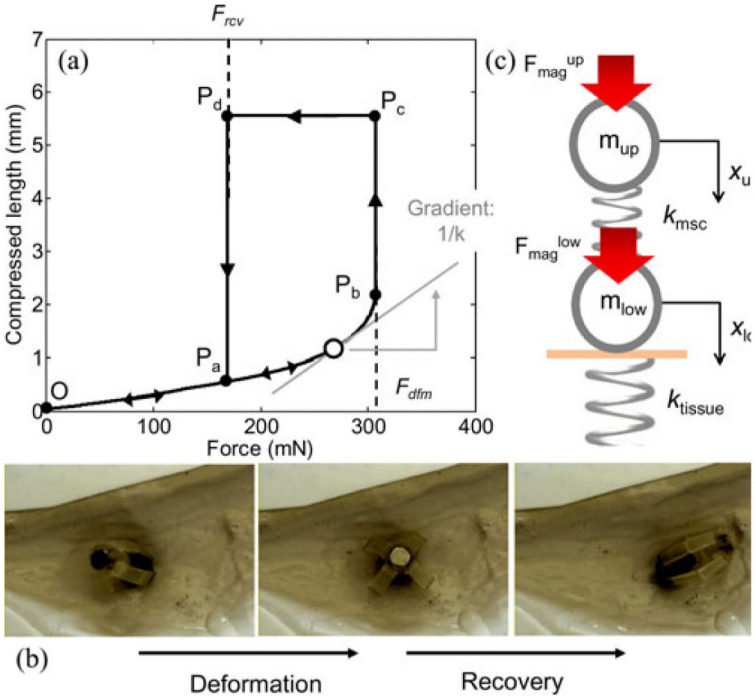

Fig. 6.

(a) Experimental shape deformation and recovery curves of MASCE [14]. MASCE is compressed by the external magnetic attraction following O-P_a-P_b-P_c. If the external magnetic attraction weakens, the shape is recovered following P_c-P_d-P_a-O. The gradient of the curve gives the compliance of MASCE at each state. (b) Snapshots of MASCE during the axial contraction and shape recovery while rolling. (c) Serially connected mass–spring system for modeling MASCE's axial deformation on a tissue.

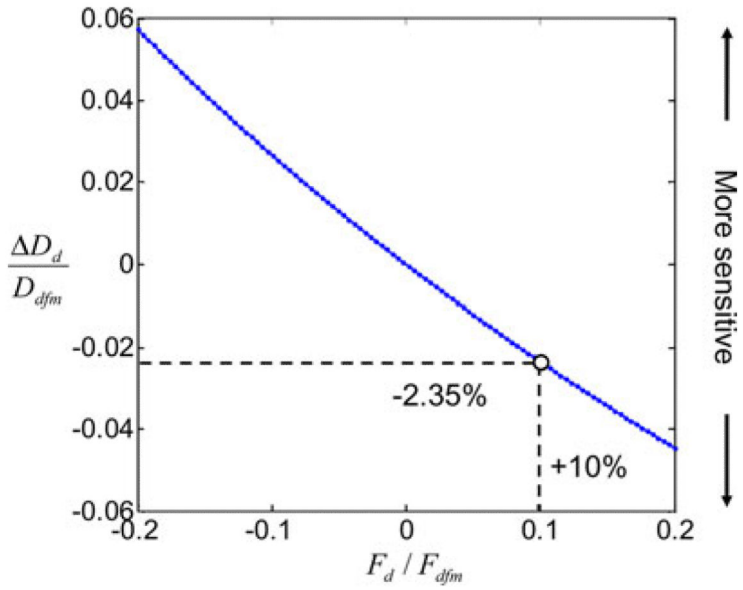

Fig. 7.

Theoretical analysis about the effect of the force disturbance on the shape deformation (or recovery) distances.

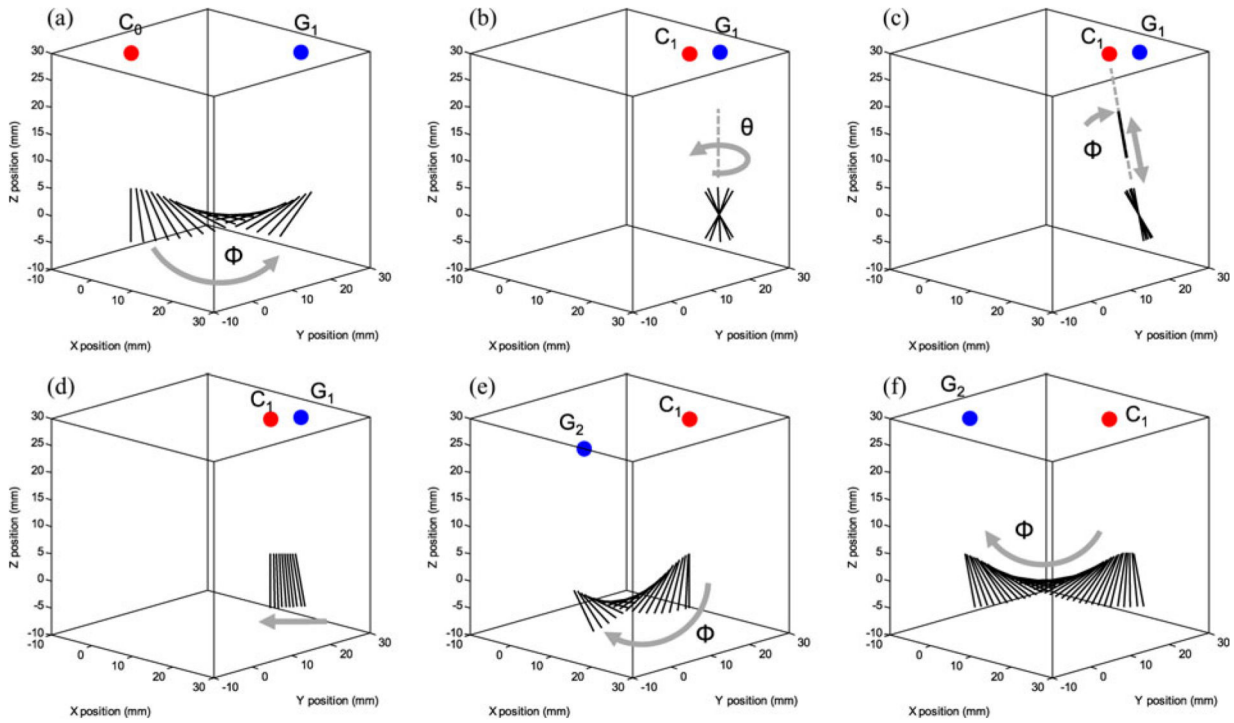

Fig. 8.

Example simulated sequential execution of rolling locomotion and 3-D localization. (a) Rolling locomotion. (b) θ alignment during the coaxial alignment. (c) Φ alignment during the coaxial alignment and shape deformation of MASCE. (d) *XY* alignment. (e) Rolling locomotion toward the second goal position. (f) Backward rolling locomotion toward the workspace. C_0 and C_1 represent the actual position of MASCE, and G_1 and G_2 represent its goal positions.

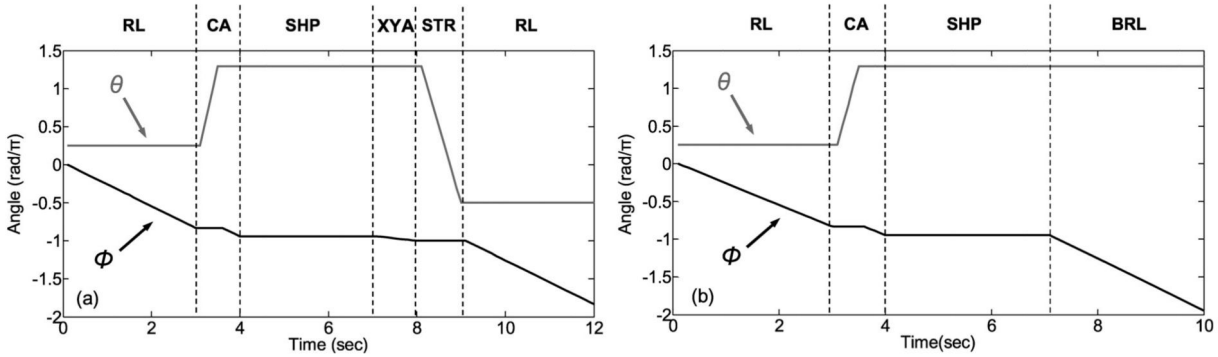

Fig. 9.

Simulated EPM's θ and Φ during the first rolling locomotion, 3-D localization, steering, and the second rolling locomotion. (a) Normal process: the first rolling locomotion (RL), coaxial alignment (CA), shape deformation (SHP), XY alignment (XYA), steering (STR), and the second rolling locomotion (RL). (b) On a slope (the boundary of the workspace), the first rolling locomotion (RL), coaxial alignment (CA), shape deformation (SHP), XY alignment (XYA), and backward rolling locomotion (BRL).

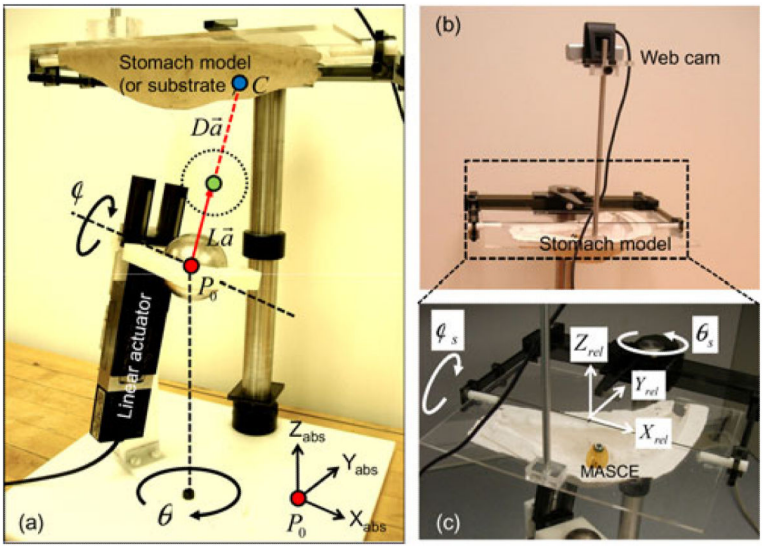

Fig. 10.

Experimental setup to evaluate the performance of the proposed 3-D localization method. (a) Lower part is the EPM manipulator part, which consists of pivots for Φ and θ rotations for the coaxial alignment stage and a linear actuator to adjust the distance in the shape deformation and recovery stage. *a* means the magnetization direction of EPM. It is determined by Φ and θ [see (2)]. (b) and (c) Upper part with five-degree-of-freedom motion stage and a webcam for image analysis. T_{abs}^{rel} is calculated based on the substrate's offset distances (x_{off} , y_{off} , z_{off}) in three axes (X_{rel}, Y_{rel}, Z_{rel}) and offset orientations (Φ_{off}, θ_{off}) about two axes (Φ_s, θ_s). *D* means D_{dfm} or D_{rcv}. *L* means L_{dfm} or L_{rcv}.

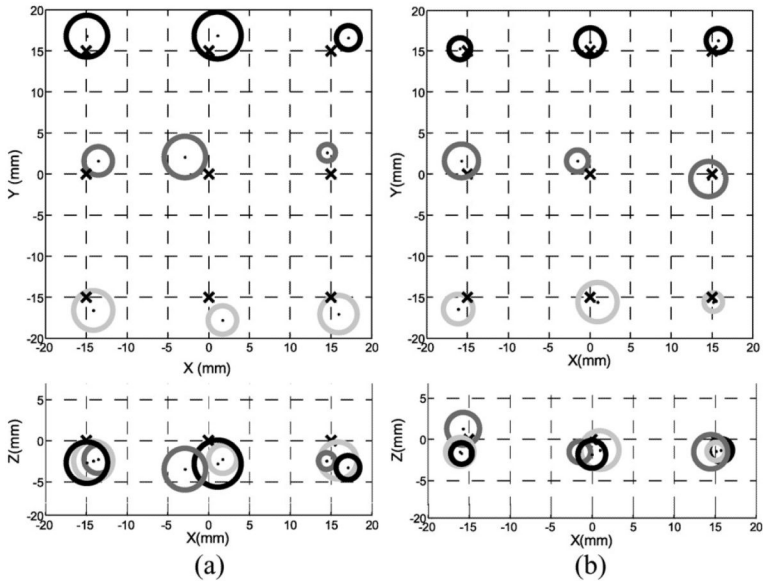

Fig. 11.

Results of 3-D localization experiments on an acrylic substrate. Comparison of the real positions and the estimated positions. (a) Shape deformation (D_{dfm})-based localization (the upper row: *XY* plane view; the lower row: XZ plane view). (b) Shape recovery (D_{rcv})-based localization.

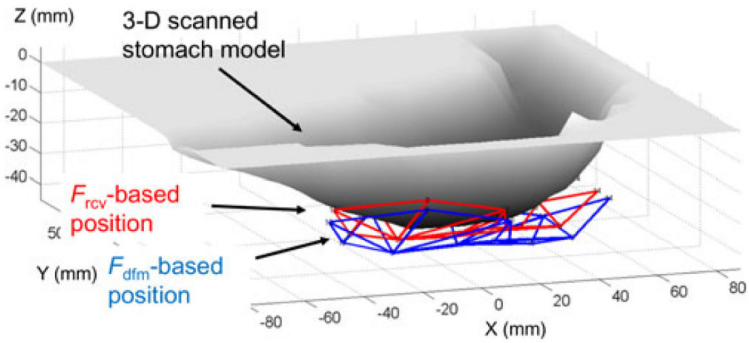

Fig. 12.

Results of 3-D localization experiments on a silicone rubber stomach model. The blue points and the red points present the localized MASCE using shape deformation and recovery, respectively.

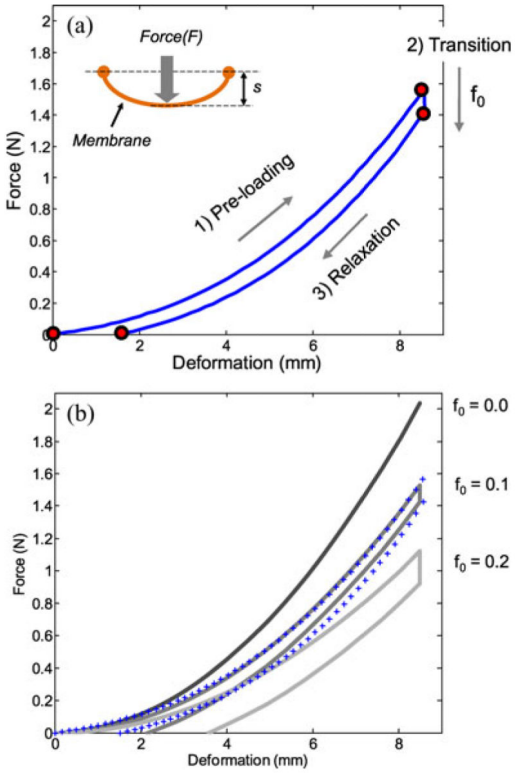

Fig. 13.

(a) Force-deformation curve of the sample A investigated by an indentation setup. (b) Reconstructed effective tissue stiffness curves. The stress relaxation of the membrane sample was differently set between 0.0 and 0.2. The dashed curve represents the indentation experiment result of the plot in (a).

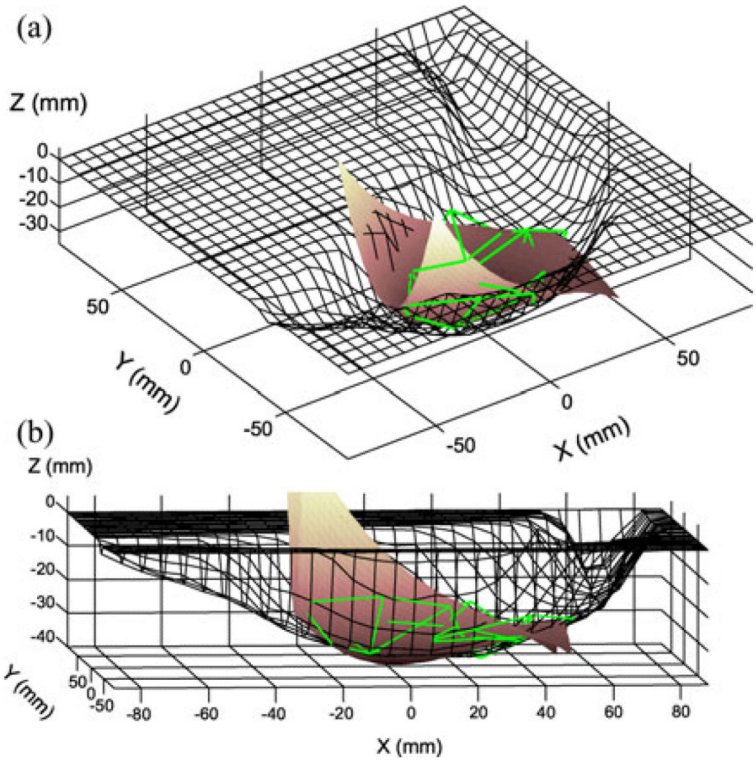

Fig. 14.

Deformation-compensated 3-D map of the synthetic stomach model (the local surface). (a) Overview of the matching results. (b) Side view of the contact points and the reconstructed 3-D geometrical model. The black mesh is the real stomach geometry. The surface with gradient is the reconstructed stomach geometry. The green linkages indicate the deformation-compensated contact points.

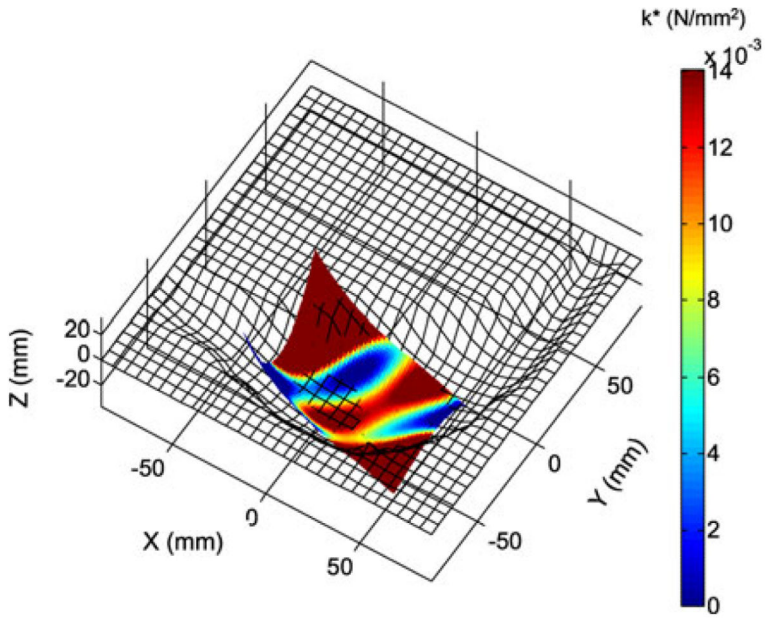

Fig. 15.

Interpolated relative stiffness coefficients on the reconstructed 3-D map. Measured local tissue compliance parameters overlapped with the reconstructed 3-D geometrical model of the synthetic stomach. The red regions show the relatively rigid areas.

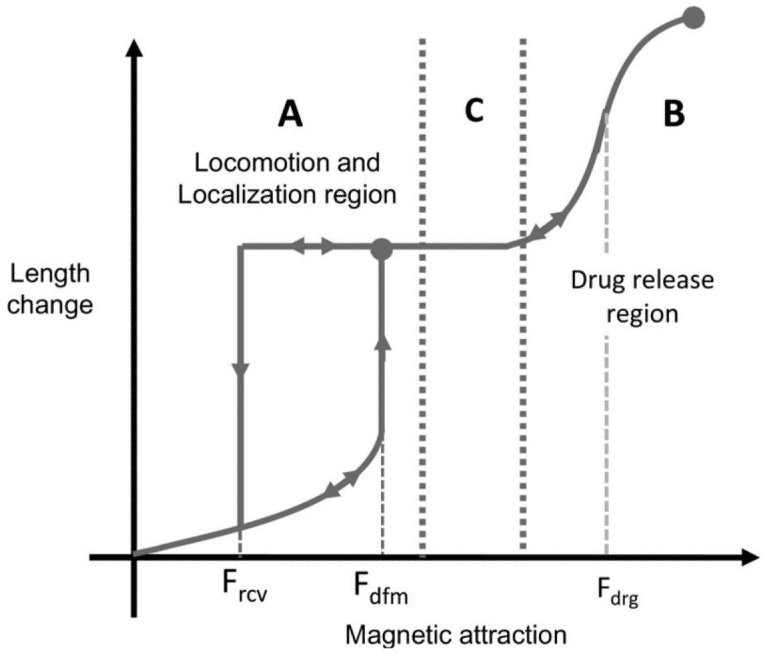

Fig. 16.

Desired shape deformation and recovery curve of MASCE during rolling locomotion and 3-D localization (region **A**), localized drug release (region **B**), and force margin preventing the undesired drug release during rolling locomotion and 3-D localization (region **C**).

TABLE I

Experimental Results of the Coaxial Alignment

MASCE direction		EPM* direction	Error
(x_c, y_c, z_c) [mm]	(Φ_c, θ_c) [°]	(Φ_{cx}, θ_{cx}) [°]	(α) [°]
(5, 1, 52)	(10, 5)	(13, 6)	5.0
(15, 7, 50)	(30, 15)	(27, 18)	4.8
(15, 12, 46)	(45, 25)	(40, 23)	3.3
(15, 21, 36)	(57, 33)	(54, 36)	4.7
(15, 28, 35)	(53, 40)	(62, 42)	7.0
(24, 31, 33)	(56, 47)	(52, 50)	5.2

*Cylindrical EPM 50 mm (diameter) × 80 mm (length).

TABLE II

Specifications of MASCE and EPM

EPM (External Permanent Magnet)	
Shape / Material	**Sphere /NdFeB (N42)**
Diameter	**50 [mm]**
Surface field	**0.882 [T]**
MASCE	
Size	
Diameter	15 mm
Length (max. / min.)	33mm / 27 mm
Internal magnets	
Shape / Material	Cylindrical / NdFeB (N52)
Diameter / Thickness	6.4 / 6.4 [mm]
Surface field	0.523 [T]
Critical force	
F_{dfm} (F_{rcv})	310(160) [mN]
Critical distance (experimental)	
D_{dfm}	44.2 (±0.24) [mm]
D_{rcv}	57.2 (±0.15) [mm]

TABLE III

Experiment Localization Error

Using shape deformation:	
Min. / Max. error	3.1 [mm]/5.0 [mm]
Average error	3.7 ± 1.8 [mm]
Using shape recovery:	
Min. / Max. error	1.5 [mm] / 2.6 [mm]
Average error	2.0 ± 1.5 [mm]

TABLE IV

Comparison of the Tissue Stiffness Coefficients

Sample	k_{cf} (N/mm^2)	f(N)	Δs (mm)	k^* (N/mm^2)	
				$f_0 = 0$	$f_0 = 0.1$
A	0.021	0.09–0.12	2.7	0.028	0.021
B	0.026	0.11–0.12	2.2	0.042	0.032
C	0.047	0.22–0.30	1.8	0.063	0.048

*F^{P}_{dfm} (measured) = 1.57 ± 0.04 N; F^{P}_{rcv} (measured) = 0.64 ± 0.01 N.